Science Bulletin 64 (2019) 301–309

Contents lists available at ScienceDirect

Science Bulletin

journal homepage: www.elsevier.com/locate/scib

Article

Interface structure prediction via CALYPSO method

Bo Gao [a,1], Pengyue Gao [a,1], Shaohua Lu [a], Jian Lv [a], Yanchao Wang [a], Yanming Ma [a,b,*]

[a] State Key Laboratory of Superhard Materials & Innovation Center for Computational Physics Methods and Softwares, College of Physics, Jilin University, Changchun 130012, China
[b] International Center of Future Science, Jilin University, Changchun 130012, China

ARTICLE INFO

Article history:
Received 4 January 2019
Received in revised form 7 February 2019
Accepted 9 February 2019
Available online 14 February 2019

Keywords:
Solid–solid interface
Structure prediction method
Lattice mismatch
TiO_2 grain boundary

ABSTRACT

The atomistic structures of solid–solid interfaces are of fundamental interests for understanding physical properties of interfacial materials. However, determination of interface structures faces a substantial challenge, both experimentally and theoretically. Here, we propose an efficient method for predicting interface structures via the generalization of our in-house developed CALYPSO method for structure prediction. We devised a lattice match toolkit that allows us to automatically search for the optimal lattice-matched superlattice for construction of the interface structures. In addition, bonding constraints (e.g., constraints on interatomic distances and coordination numbers of atoms) are imposed to generate better starting interface structures by taking advantages of the known bonding environment derived from the stable bulk phases. The interface structures evolve by following interfacially confined swarm intelligence algorithm, which is known to be efficient for exploration of potential energy surface. The method was validated by correctly predicting a number of known interface structures with only given information of two parent solids. The application of the developed method leads to prediction of two unknown grain boundary (GB) structures (r-GB and p-GB) of rutile TiO_2 $\Sigma5(2\,1\,0)$ under an O reducing atmosphere that contained Ti^{3+} as the result of O defects. Further calculations revealed that the intrinsic band gap of p-GB is reduced to 0.7 eV owing to substantial broadening of the Ti-3*d* interfacial levels from Ti^{3+} centers. Our results demonstrated that introduction of grain boundaries is an effective strategy to engineer the electronic properties and thus enhance the visible-light photoactivity of TiO_2.

1. Introduction

Solid–solid interfaces or grain boundaries (GB) widely exist in a broad range of materials such as heterojunctions and polycrystalline materials, and they often play a significant role in governing the physical properties of solids. For example, it is a rare event to have the coexistence of superconductivity and ferromagnetism that appear, however, in a heterojunction interface formed by $SrTiO_3$ and $LaAlO_3$ [1,2]. Moreover, interfaces play a decisive role in determining the performance of many devices [3,4]. For instance, since the interfacial resistance between the electrode and electrolyte in all-solid-state lithium batteries is so substantial, it has become a bottleneck delaying further improvement of the battery performance [4], whereas silicon can exhibit improved photovoltaic performance owing to the presence of GBs [5]. Therefore, investigation of the effects of interfaces or GBs is of significant fundamental interest and practical importance [5,6].

The properties of materials depend strongly on the atomistic structure; therefore, determination of the structure is the critical step toward an in-depth understanding of a material's properties. High-resolution transmission electron microscopy has been used to investigate the structures of interfaces [7,8]. However, it provides only information about the surface atoms but not on the atomic configurations inside the materials. This is the reason why experimental studies often failed especially for complicated interfacial systems. There is an apparent need to develop theoretical methods in aiding the experimental determination of the interface structure. However, it remains a major challenge since the structures of interfaces depend strongly on a number of variables (e.g., the crystal orientation, lattice mismatch [9], and low symmetric features [7], etc), despite the fact that a number of theoretical methods (e.g., molecular dynamics [10], genetic algorithms [11,12], differential evolution [13], random sampling [14], evolutionary algorithms [15], and machine learning [16]) have been proposed and applied to the research on the interface structures of several examples (e.g., graphene, Cu, and $SrTiO_3$).

In this manuscript, we propose a robust and generalized method for predicting structures of solid–solid interfaces via the CALYPSO method [17–21] on structure prediction, which has been

* Corresponding author.
E-mail address: mym@jlu.edu.cn (Y. Ma).
[1] These authors contributed equally to this work.

https://doi.org/10.1016/j.scib.2019.02.009
2095-9273/

applied into prediction of a variety of structures (e.g., 2D [22,23] and 3D crystals [24], 0D clusters [25,26] as well as surface reconstruction [27] and adsorption [28]). The method will be detailed in the method section and is validated by reproducing known interface structures of armchair-zigzag graphene GBs and Σ3 (1 1 2) GBs of rutile TiO_2. The application of the developed method leads to the prediction of two energetically favorable structures in Σ5(2 1 0) GBs of rutile TiO_2 with narrow band gaps under an O reducing atmosphere, which are useful for the visible-light photoactivity of TiO_2.

2. Method and implementation

We developed two structure models for the simulation of solid-solid interfaces as shown in Fig. 1a and b. One is a slab model (Fig. 1a), which consists of four regions: a vacuum region, two bulk phase regions, and an interface region. The bulk phase regions preserve the crystal structures of both materials, and the atomistic structure in the interface region evolves following the CALYPSO method. This model has many advantages, the most obvious being its simplicity and ubiquity. However, the undesirable surface states induced from the top and bottom surfaces of the slab exposed to vacuum substantially affect the accuracy of the simulation of the intrinsic interfacial properties. This effect cannot be negligible even if a large simulated cell of bulk phase regions is adopted or the surface is passivated by the adsorbed atoms in some systems.

To eliminate surface state effects, a model without the vacuum of the interface (Fig. 1b) is also employed in our method. This model has two bulk phase regions and two equivalent interfaces in the simulated cell. The bulk phase regions must be sufficiently thick to ensure that the interactions between the two equivalent interfaces are negligible. The key shortcoming of this model is that it can only be applied to the interface system whose two bulk phase regions possess mirror or inversion symmetry. Both models were implemented using the CALYPSO method, and a suitable interface model should be selected before the prediction of interface structures.

Generally, a simulated interface model consists of two (*A* and *B*) bulk phase regions and an interface region. The ultimate goal of structure prediction is to identify the global energy minimum of the interface model among a large number of local minima. The total energy of the interface model (E_{total}) can be written as

$$E_{\text{total}} = E_{\text{bulk}}(A) + E_{\text{bulk}}(B) + E_{\text{interface}}, \tag{1}$$

where $E_{\text{bulk}}(A)$, $E_{\text{bulk}}(B)$, and $E_{\text{interface}}$ are the energies of structures in *A* and *B* bulk regions, and the interface region, respectively. Especially, the lattices of the *A* and *B* phases are not identical in most interface systems. Lattice deformations should be performed to adjust *A* and *B* lattices to satisfy the common lattice of the model. Inevitably, lattice strains are introduced and result in an additional contribution to the bulk energies in the model. Therefore, the structure energy in the bulk phase region can be represented by

$$E_{\text{bulk}} = E_{\text{bulk}}^{\text{ideal}} + E_{\text{bulk}}^{\text{strain}}, \tag{2}$$

where $E_{\text{bulk}}^{\text{ideal}}$ and $E_{\text{bulk}}^{\text{strain}}$ are the energy of the ideal bulk crystal and the bulk strain energy induced from the lattice mismatch between *A* and *B* phases. Including the bulk strain energy, the total energy of the interface model becomes

$$E_{\text{total}} = E_{\text{bulk}}^{\text{ideal}}(A) + E_{\text{bulk}}^{\text{ideal}}(B) + E_{\text{bulk}}^{\text{strain}}(A) + E_{\text{bulk}}^{\text{strain}}(B) + E_{\text{interface}}. \tag{3}$$

The energies of the ideal bulk crystals of $E_{\text{bulk}}^{\text{ideal}}(A)$ and $E_{\text{bulk}}^{\text{ideal}}(B)$ are invariable with the simulated interface model. Therefore, both the bulk strain energies ($E_{\text{bulk}}^{\text{strain}}(A)$ and $E_{\text{bulk}}^{\text{strain}}(B)$) and the interface structure energy ($E_{\text{interface}}$) must be minimized for the prediction of ground state interface structure.

The CALYPSO interface structure prediction method has been developed based on the requirements of energy minimization of interface model. The flow chart shown in Fig. 1c consists of three main parts. First, an automatic search for a superlattice with minimal lattice-mismatch strain between the two bulk materials is performed using a lattice match toolkit. Second, the local atomistic structures at interface region in the lattice-matched model are initially generated under the bonding constraints. Finally, the local interface structures evolve from the current low-energy interface configurations by following the interfacially confined particle swarm optimization (PSO) algorithm. After the initial generation and evolution of structures, all the models are geometrically relaxed using *ab initio* or empirical potential methods. In addition, a rigid-body displacement between two bulk phases parallel to the interface plane has been regarded as a search dimension in the structure prediction to cover the entire search space.

2.1. Lattice matching

As described, the mismatched lattices of two bulk materials usually induce the bulk strain energies and even affect the local atomic structure at the interface (e.g., introduction of defects and dislocations) [29]. Thus, a commensurate lattice is key for the prediction of the stable interface structure. However, finding a coincident superlattice manually is extremely complicated because of the tremendous possible combinations between the superlattices of the two bulks [30–33]. Here, we present a general and robust scheme to automatically search for the coincident superlattices for given crystallographic unit cells of two materials. Note that the advantage of our scheme is that it only needs the unit cells instead of the specific surface vectors used in previous approaches [30,32].

Fig. 2 shows the detailed screening procedure to search for the lattice-matched superlattice of our scheme. It is started from the crystallographic unit cells of two (*A* and *B*) materials. For each material, the surfaces are created based on the Miller indices. Since exhausting all the surfaces with infinite Miller indices is impossible, a rational threshold is introduced. All the Miller indices less than the threshold are generated and reduced to irreducible Miller indices. Then, the symmetry operations belonging to the space group of the crystal structure are performed on the created surfaces to eliminate the symmetric equivalent surfaces. The primitive vectors of the nonequivalent surfaces for two materials, ($\vec{u}_{P,A}, \vec{v}_{P,A}$) and ($\vec{u}_{P,B}, \vec{v}_{P,B}$), are preserved in two groups, respectively.

For each nonequivalent surface of the *A* or *B* materials, the superlattice vectors ($\vec{u}_A, \vec{v}_A$) or ($\vec{u}_B, \vec{v}_B$) are constructed based on the primitive vectors and the possible matrix notations (*M* or *N*) [34] using the formulas

$$\begin{bmatrix} \vec{u}_A \\ \vec{v}_A \end{bmatrix} = M \cdot \begin{bmatrix} \vec{u}_{P,A} \\ \vec{v}_{P,A} \end{bmatrix}, \tag{4}$$

$$\begin{bmatrix} \vec{u}_B \\ \vec{v}_B \end{bmatrix} = N \cdot \begin{bmatrix} \vec{u}_{P,B} \\ \vec{v}_{P,B} \end{bmatrix}, \tag{5}$$

where *M* and *N* are 2×2 square matrices with integral matrix elements. Here, the superlattices that do not obey the right-hand rule should be discarded. Considering the high computational cost of the "brute force" approach to exhaust all the possible superlattices, a rational threshold area is used to confine the size of the superlattice.

Then, the lattice-mismatch strain between the superlattices of *A* and *B* materials are evaluated. Here, the *B* material is supposed to have larger elastic modulus than the *A* material so that the super-

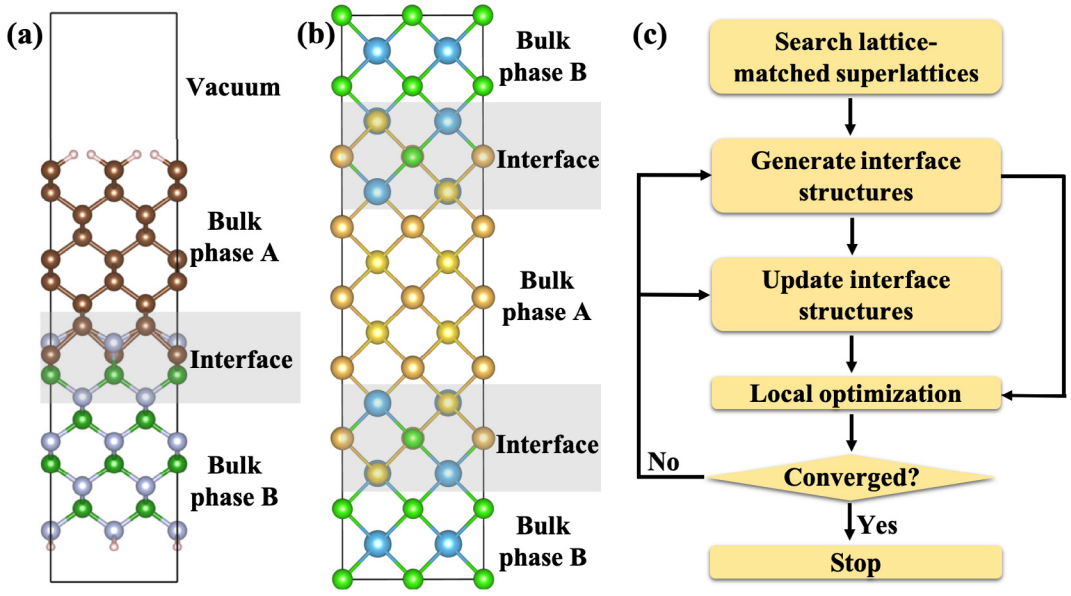

Fig. 1. (Color online) Two simulated models adopted in our method. (a) Slab model with an interface region, two bulk phase regions, and vacuum in unit cell. (b) Model with two equivalent interface regions and two bulk phase regions in simulated cell. (c) Flow chart of interface structure prediction method based on CALYPSO method.

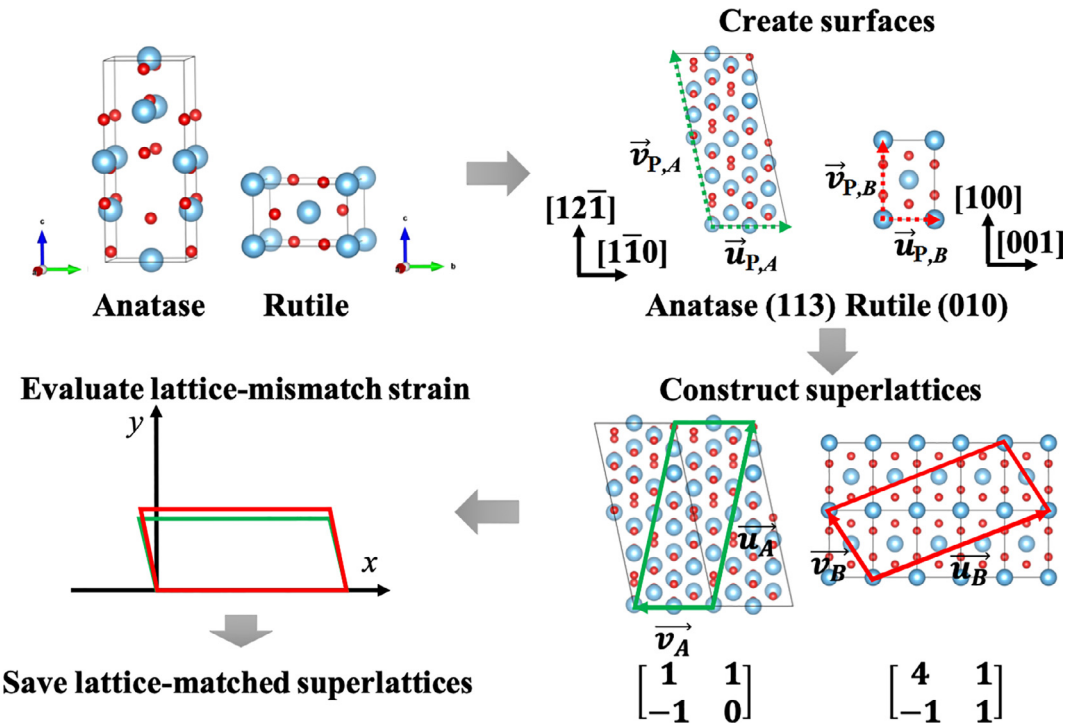

Fig. 2. (Color online) Flow path of lattice match toolkit. The optimal lattice-matched superlattice for the TiO_2 rutile and anatase phases shown in Table 1 was taken as the example. The blue and red spheres represent Ti and O atoms, respectively.

lattice of the *A* material is deformed to match the superlattice of the *B* material. The strain tensor ε in deformed *A* material is a symmetric matrix, and defined as [30],

$$\varepsilon = \begin{bmatrix} \varepsilon_{xx} & \varepsilon_{xy} \\ \varepsilon_{yx} & \varepsilon_{yy} \end{bmatrix}. \tag{6}$$

Here a unified coordinate system is introduced, and the vectors of the superlattice, $(\vec{u}_A, \vec{v}_A)$ and $(\vec{u}_B, \vec{v}_B)$, are rationally rotated to ensure that $\vec{u}_A$ and $\vec{u}_B$ are aligned along the *x*-axis to simplify the calculation of the strain tensor, meaning that $u_{A,y} = u_{B,y} = 0$. A 2×2 square matrix *e* is introduced to applied on the *A* superlattice to match the *B* superlattice,

$$e \cdot (\vec{u}_A, \vec{v}_A) = (\vec{u}_B, \vec{v}_B), \tag{7}$$

and strain tensor ε is derived from *e* using,

$$\varepsilon = \frac{1}{2}(e + e^{\mathrm{T}}) - I. \tag{8}$$

The components of ε can be solved from Eqs. (6)–(8), so that

$$\varepsilon_{xx} = \frac{u_{B,x} - u_{A,x}}{u_{A,x}}, \tag{9}$$

$$\varepsilon_{yy} = \frac{v_{B,y} - v_{A,y}}{v_{A,y}}, \tag{10}$$

$$\varepsilon_{xy} = \varepsilon_{yx} = \frac{1}{2}\left(\frac{v_{B,x}}{v_{A,y}} - \frac{u_{B,x}v_{A,x}}{u_{A,x}v_{A,y}}\right). \tag{11}$$

In our scheme, the numerical average $\bar{\varepsilon}$ of the absolute values of the strain tensor components [30] is used to quantify the lattice mismatch:

$$\bar{\varepsilon} = \frac{|\varepsilon_{xx}| + |\varepsilon_{yy}| + 2|\varepsilon_{xy}|}{4}. \tag{12}$$

The pairs of *A* and *B* superlattices with small values of $\bar{\varepsilon}$ are preserved as well-matched superlattices.

To demonstrate the performance of our scheme, we applied it to find the pairs of superlattices with small lattice mismatch for the TiO_2 anatase and rutile heterointerface, which has been proved to effectively enhance the photocatalytic properties of TiO_2 [35]. As shown in Table 1, a number of well-matched superlattices have been successfully discovered, whose average values of the lattice mismatch strain tensors $\bar{\varepsilon}$ are much lower than that of the previously proposed anatase(1 0 1)/rutile(1 1 1) heterointerface [35]. These results clearly demonstrate the reliability of our lattice-match toolkit.

2.2. Structure generation under the bonding constraints

Once the coincident lattice for two materials has been obtained, the initial interface structures including the atomic coordinates at the interface region and the rigid-body displacements between two bulk phases will be generated. It is generally accepted that the thermodynamic stabilities of materials are strongly dependent on the local bonding environments of the atomic coordination number and interatomic distance [36]. Based on the crystal field theory, transition-metal cations usually coordinate with a certain number of ligands forming a polyhedron to lower the energy, such as the stable rutile and anatase TiO_2 structures, in which a Ti atom is surrounded by six O atoms forming an octahedron. Besides, in covalent systems, an atom usually bonds with a certain number of surrounding atoms because of the hybridization of orbitals. For instance, the C atoms are three-coordinated in the bulk phase and GBs of graphene because of sp^2 hybridization [13]. Therefore, the local bonding environments derived from the stable bulk structures are employed as constraints to generate the atomic interface structures in our method. It should be emphasized that the interatomic distance and atomic coordination numbers are confined into an appropriate range instead of adopting strict criteria induced from the bulk phase.

The detailed procedure for the structure generation with bonding constraints is described in the following. Initially, the position of an interfacial atom is randomly generated in the interface region, and then, rationality is examined by calculating the interatomic bond lengths and nearest-neighbor coordination numbers. If the interatomic bonds are shorter than the required lengths or the atomic coordination numbers are beyond the requirement, the generated atomic position is discarded and regenerated until a physically justified atomic position is accepted. This procedure is repeated iteratively until a physically justified interface structure is completely constructed.

To evaluate the performance of the bonding constraints, it was applied to two illustrative examples of the armchair-zigzag graphene GB [14] and stoichiometric Σ3(1 1 2) GB of rutile TiO_2 [7]. For each example, 500 interface structures were randomly generated with and without the bonding constraints and then optimized using the density-functional-based tight binding (DFTB+) software package. The obtained energetic distributions of these structures for two examples are presented in Fig. 3a and b, respectively. The results indicate that the interface atomic structures generated with bonding constraints are generally more energetically favorable than those generated without bonding constraints, especially for the complicated Σ3(1 1 2) GB of rutile TiO_2. More importantly, the experimental structure of Σ3(1 1 2) GB of rutile TiO_2 was indeed generated within 500 structures when employing bonding constraints; however, this structure was not found without bonding constraints. Therefore, the use of bonding constraints to generate the initial interface structures plays a critical role in the prediction of complicated interface structures.

2.3. Structure evolution via the interfacially confined PSO algorithm

Once the initial structures were generated, the geometry relaxation was performed to drive them to local minima on the potential energy landscape. Here the static energies obtained using *ab initio* or empirical potential methods were regarded as the fitness of the structures. To explore the entire potential energy landscape, the structures evolve by following the interfacially confined

Table 1
Lattice-matched superlattices for anatase and rutile TiO_2 heterojunction.[a]

Anatase					Rutile					$\bar{\varepsilon}$(%)
Indices	*M*	$\lvert\vec{u}\rvert$	$\lvert\vec{v}\rvert$	γ	Indices	*N*	$\lvert\vec{u}\rvert$	$\lvert\vec{v}\rvert$	γ	
(1 1 3)	$\begin{bmatrix} 1 & 1 \\ -1 & 0 \end{bmatrix}$	13.05	5.52	102.21	(0 1 0)	$\begin{bmatrix} 4 & 1 \\ -1 & 1 \end{bmatrix}$	13.05	5.60	101.87	0.46
(0 0 1)	$\begin{bmatrix} -1 & 4 \\ -1 & -1 \end{bmatrix}$	16.09	5.52	120.96	(1 $\bar{5}$ 1)	$\begin{bmatrix} 2 & 1 \\ -1 & 0 \end{bmatrix}$	16.05	5.60	122.01	0.84
(1 2 1)	$\begin{bmatrix} 1 & 0 \\ 1 & 2 \end{bmatrix}$	5.58	15.63	80.39	(2 5 2)	$\begin{bmatrix} 0 & 1 \\ -1 & 0 \end{bmatrix}$	5.60	16.08	80.39	0.89
(1 1 0)	$\begin{bmatrix} -1 & -1 \\ -1 & 1 \end{bmatrix}$	9.60	5.58	90.71	(0 1 1)	$\begin{bmatrix} 2 & 0 \\ 0 & 1 \end{bmatrix}$	9.39	5.60	90	0.91
(1 0 1)	$\begin{bmatrix} 3 & 0 \\ 0 & 1 \end{bmatrix}$	11.71	5.58	110.47	(1 1 1)	$\begin{bmatrix} 0 & -2 \\ 1 & 0 \end{bmatrix}$	11.19	5.60	107.2	2.67

[a] Here, indices represent the Miller indices for the anatase and rutile phases. *M* and *N* refer to the matrix notations for constructing superlattice of anatase and rutile as defined in Eqs. (4) and (5), respectively. $\lvert\vec{u}\rvert$ and $\lvert\vec{v}\rvert$ represent the length of the vectors of superlattices, which are given in Å. γ is the angle between the two vectors. $\bar{\varepsilon}$ represents numerical average of the absolute values of the lattice-mismatch strain tensor. The components of Miller indices were confined in the range from –5 to 5, and the maximum area of the superlattice was set to 100 Å^2. Here the lattice parameters of the anatase phase are $a = b = 3.90$ Å, $c = 9.70$ Å. The lattice parameters of the rutile phase are $a = b = 4.70$ Å, $c = 3.04$ Å. The superlattices of anatase(1 0 1)/rutile(1 1 1) heterointerface proposed by Ju et al. [35] and reproduced by our lattice match toolkit was listed for comparison.

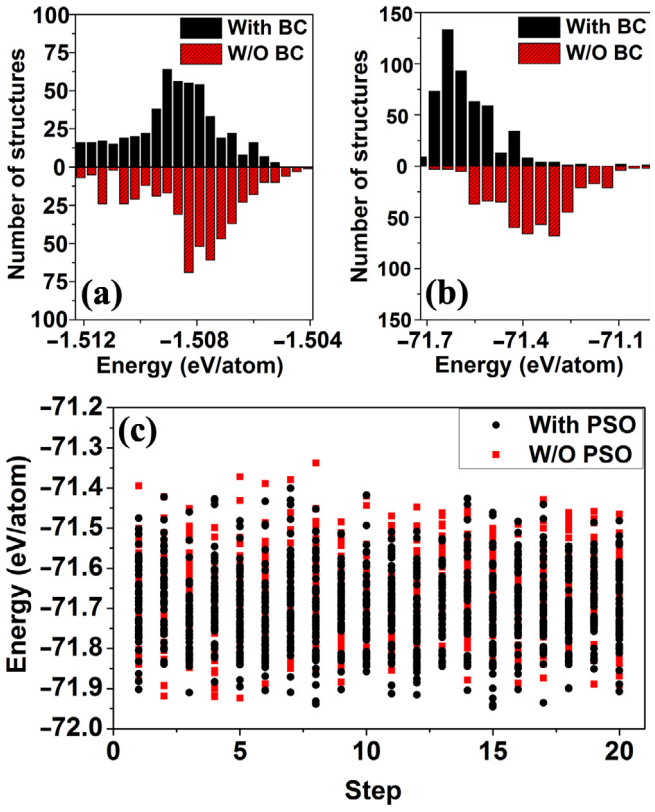

Fig. 3. (Color online) Test results of the developed techniques in the interface structure prediction method. (a) Energetic distributions of 500 structures for graphene armchair-zigzag GB with and without bonding constraints (BC). (b) Energetic distributions of 500 structures for the stoichiometric Σ3(1 1 2) GB of rutile TiO_2 generated with and without BC. (c) History of energies of structures in two individual structure searches with 60% structures evolving with PSO and without PSO. The population size for each generation was set as 50.

PSO algorithm [17] with global searching capability. Supposing that the interface region contains n atoms, $3n + 2$ search dimensions ($3n$ dimensions for the atomic coordinates and 2 dimensions for the rigid-body displacement) are required to be updated in an interface structure. In particular, the position of structure (x) in each search dimension k was updated according to

$$x_i^{t+1}(k) = x_i^t(k) + v_i^{t+1}(k), \tag{13}$$

where i and t are the indices of the structure in the population and the generation, respectively. The velocities v of the structures in the first generation were generated randomly. The new velocity of each individual i in the k^{th} dimension was calculated based on its previous location (x) before optimization, its previous velocity (v), its current location ($pbest_i^t$) with the best fitness achieved for this individual, and the global location ($gbest$) with the overall best fitness value using

$$v_i^{t+1}(k) = \omega v_i^t(k) + c_1 r_1 \left[pbest_i^t(k) - x_i^t(k)\right] + c_2 r_2 \left[gbest(k) - x_i^t(k)\right]. \tag{14}$$

The inertia weight of ω dynamically and linearly decreased from 0.9 to 0.4 during the iteration. c_1 and c_2 denoting the learning factors were fixed at 2 in our method. r_1 and r_2 were two random numbers uniformly distributed in the range [0, 1]. To avoid the prematurity of the algorithm, the velocities were confined within the range from $-1.2/l$ to $1.2/l$, where l (in Å) was the length of the corresponding lattice vector. To improve the efficiency of the procedure and enhance the structural diversity, a proportion of low-energy structures of the previous generation were selected to produce the next generation using PSO; the other structures were randomly generated.

To illustrate the effectiveness of PSO algorithm, we performed two individual predictions of stoichiometric Σ3(1 1 2) GB of rutile TiO_2. For one test, 60% of the structures for each population were generated using the PSO algorithm, whereas for the other test, all the structures were randomly generated. The maximum iterations and population size of each generation for both tests were set to 20 and 50, respectively. All the structures were optimized using DFTB + software. The history of the evolution of the structural energy is shown in Fig. 3c. It is apparent that most structures generated using PSO were distributed in the low-energy region. It is also noteworthy that the energetically stable interface structure was identified in the 15th generation using the PSO algorithm; however, it could not be observed within 20 generations using the fully random method.

3. Applications and results

3.1. Computational details

We implemented all the schemes for interface structure prediction into the CALYPSO software and applied it to investigate the structures of graphene armchair-zigzag GBs and rutile TiO_2 GBs. For the graphene armchair-zigzag GB, a (7,0)|(4,4)-type GB model with a lattice mismatch strain of 1.0% was adopted. The slab model contains 111 C atoms per simulated cell, and were separated by at least 15 Å of vacuum layer. The top and bottom surfaces exposed in the vacuum were passivated by H atoms. The non-self-consistent charge density functional tight-binding method (non-SCC-DFTB) as implemented in DFTB+ [37] was employed for local optimization of the structure search. The Slater–Koster parameters for the C–C, C–H, and H–H interactions from Ref. [38] were adopted. Accurate energetic calculations were performed using density-functional theory framework as implemented in the Vienna Ab initio Simulation Package (VASP) [39]. The Perdew–Burke–Ernzerhof generalized gradient approximation was selected for the exchange–correlation functional. The electron–ion interaction was described by projector-augmented-wave potentials [40] with the $1s$ and $2s^2 2p^2$ configurations treated as valence electrons for H and C, respectively. A kinetic cutoff energy of 500 eV and Monkhorst–Pack k meshes with a grid spacing of 0.2 $Å^{-1}$ in reciprocal space were then adopted to ensure that the energy converged to better than 1 meV/atom.

For the rutile TiO_2 GBs, the models without vacuum and the slab models were adopted for Σ3(1 1 2) GB and Σ5(2 1 0) GB in the structure predictions, respectively. Especially for Σ5(2 1 0) GB, the slab models consisting of about 110 atoms with a thickness of above 3 nm and at least 15 Å of vacuum layer were adopted. The H atoms with 4/3 and 2/3 valence electrons were used to passivate the dangling bonds of Ti and O on the top and bottom surfaces of the slab, respectively. During the structure search, local optimization was performed using a non-SCC-DFTB method adopting the Slater–Koster parameters of the Ti–Ti, Ti–O, and O–O interactions from Ref. [41]. For the accurate energetic calculations using VASP, the $3d^2 4s^2$ and $2s^2 2p^4$ configurations were treated as valence electrons for Ti and O, respectively. The plane-wave pseudopotential method with a kinetic-energy cutoff energy of 800 eV and k-spacings of 0.25 $Å^{-1}$ in reciprocal space was employed to ensure that the energy converged to better than 1 meV/atom. The Hubbard U (U_{Ti} = 4.2 eV) parameter for Ti $3d$ states was obtained from previous work fitted to spectroscopic properties of surface oxygen vacancies at the TiO_2 rutile (1 1 0) surface [42]. The spin polarization was included in the calculation. The opti-

mized lattice parameters of the TiO_2 rutile bulk phase were $a = 4.695$ Å and $c = 3.044$ Å, which are in good agreement with experimental data [43]. Molecular dynamic (MD) simulations for Σ5(2 1 0) GB were performed in the canonical (*NVT*) ensemble at 300 K, with a time step of 0.5 fs, and the $1 \times 3 \times 1$ supercell was used in the MD simulation. The kinetic-energy cutoff was set at 500 eV, and the Γ point was used for the Brillouin zone sampling in MD simulation.

3.2. Graphene armchair-zigzag GB

We first applied our method to the 2D interface system of the graphene armchair-zigzag GB, and the predicted low-energy structures and their formation energies were shown in Fig. 4. Three known structures labeled as GB-I, GB-II, and GB-III [13,14,44] were successfully reproduced, validating the reliability of our approach for predicting the 2D interface structures. Our accurate calculations indicate that GB-III is the most energetically stable structure, with the GB-II and GB-I structures being less energetically favorable than GB-III by 2 and 100 meV/Å, respectively. The results are consistent with previous calculations [13,14]. Moreover, a new metastable GB structure, GB-IV, was predicted to be more energetically favorable than GB-I by 14 meV/Å. In GB-II, GB-III, and GB-IV, a sinuous interface is formed by alternative arrangement of the pentagons and heptagons. Despite the similarity of the structural topologies of GB-II and GB-IV with that of the stable structure of GB-III, the different spatial arrangements of heptagons lead to different thermodynamic stabilities.

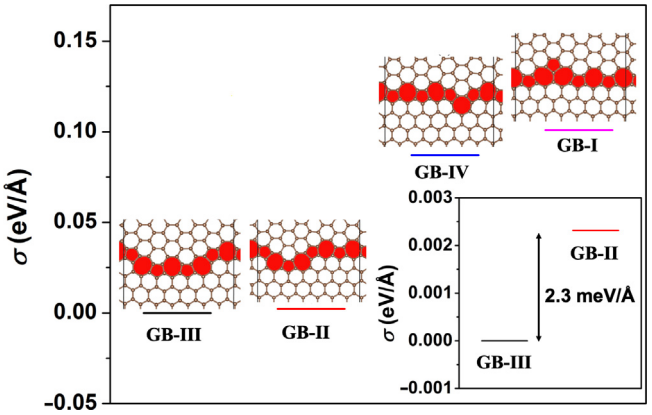

Fig. 4. (Color online) Interface formation energies (σ) and structures of GB-I, GB-II and GB-III, and GB-IV in graphene armchair-zigzag GB. σ is defined as: $\sigma = (E_{total} - E_{ref})/l_{interface}$. E_{total} and E_{ref} are the total energies of interface model and reference model. $l_{interface}$ is the length of the interface in a simulated cell. Here GB-III was chosen as the reference.

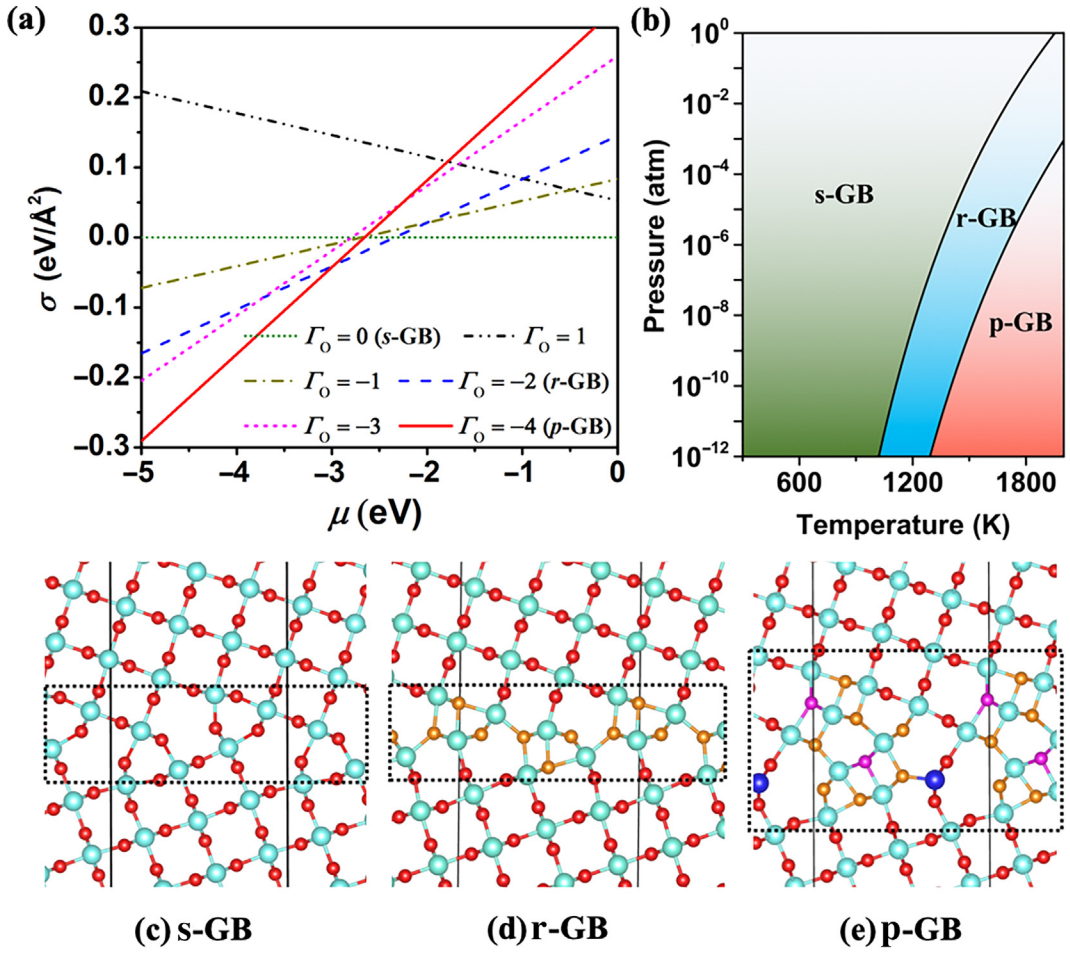

Fig. 5. (Color online) Calculation results of Σ5(2 1 0) GB of rutile TiO_2. (a) Relative formation energies (σ) of selected phases as a function of μ for Σ5(2 1 0) GB of rutile TiO_2. (b) Phase diagram of Σ5(2 1 0) GB of rutile TiO_2 as a function of temperature and O partial pressure. Stable structures of (c) s-GB, (d) r-GB, and (e) p-GB Σ5(2 1 0) GB of rutile TiO_2. The light and dark blue balls represent six- and five-coordinated Ti, respectively. The red, orange, and pink balls represent three-, four-, and five-coordinated O atoms, respectively.

3.3. Rutile TiO_2 GBs

Because of its high chemical stability, nontoxicity, and high photo-reactivity, TiO_2 has been extensively investigated as a promising photocatalyst. However, the photoreaction efficiency of TiO_2 is severely limited by its large intrinsic band gap (>3 eV). Various approaches including noble metal loading [45], doping with nonmetal atoms [46], hydrogenation [47], and surface modification [48] have been used in attempts to narrow the band gap and enhance the visible-light photoactivity of TiO_2. Recently, the introduction of Ti^{3+} originating from O defects in reduced TiO_2 has been shown to be an effective strategy to improve the photocatalytic performance [49,50]. In fact, the O defects and Ti^{3+} may widely exist at GBs in the reduced polycrystalline TiO_2 [51], leading to a beneficial influence on the photoactivity performance. However, previous studies on the GBs with stoichiometry did not observe the existence of O defects or Ti^{3+} [52,53]; therefore, our study mainly focused on TiO_2 GBs with nonstoichiometry.

We first applied our method to investigate the Σ3(1 1 2) GB of rutile TiO_2. Three previously proposed stable structures, *o*-GB, *v*-GB, and *r*-GB (Fig. S1 online) [7], were successfully reproduced, demonstrating the high reliability of our method in TiO_2 GB systems. As a typical representative of high-angle GBs, the Σ5(2 1 0) GB has attracted significant attention [54–56]. However, only a stoichiometric structure was proposed [54], and knowledge of the chemical space with non-stoichiometry remains limited. Here, we utilized our method to systematically investigate the structures of the Σ5(2 1 0) GB system with variable stoichiometry.

To determine the stability of the predicted GB structures, the relative formation energy (σ) was defined as

$$\sigma = \frac{1}{S}\left[E_{\text{interf}} - E_{\text{ref}} - (n_{\text{Ti}} - n_{\text{Ti-ref}})\mu_{\text{Ti}} - (n_{\text{O}} - n_{\text{O-ref}})\mu_{\text{O}}\right], \quad (15)$$

where S represented the interface area per simulated cell; E_{interf} and E_{ref} were the total energies of the simulated and reference models, respectively; (n_{Ti}, n_{O}) and ($n_{\text{Ti-ref}}$, $n_{\text{O-ref}}$) represented the number of Ti and O atoms in the model and reference structure, respectively; and μ_{Ti} and μ_{O} were the chemical potentials of Ti and O, respectively. Note that these parameters should satisfy the following equation: $\mu_{\text{Ti}} + 2\mu_{\text{O}} = E_{\text{Ti(bulk)}} + 2E_{\text{O(O}_2\text{)}} + \Delta H_{\text{f}}(\text{TiO}_2)$, where $E_{\text{Ti(bulk)}}$ and $E_{\text{O(O}_2\text{)}}$ denoted the total energies per atom of metal Ti bulk phase and gaseous O_2, respectively. $\Delta H_{\text{f}}(\text{TiO}_2)$ represented the formation enthalpy of rutile TiO_2. Here, the O chemical potential with respect to the energy of gaseous O_2 was defined as $\mu = \mu_{\text{O}} - E_{\text{O(O}_2\text{)}}$, which was taken as a variable of σ, spanning a range from $\Delta H_{\text{f}}(\text{TiO}_2)$ (Ti-rich) to 0 (O-rich). The excess of O with respect to Ti at GB was defined as $\Gamma_{\text{O}} = n_{\text{O}} - 2n_{\text{Ti}}$.

Our method successfully reproduced the known stoichiometric GB structure (s-GB), and two novel nonstoichiometric GB structures named as r-GB and p-GB were predicted in the range of low chemical potential of O. The calculated formation energies (σ) of the low-energy GB structures with respect to s-GB were depicted in Fig. 5a. The stability ranges of μ for r-GB and p-GB were from −3.0 to −2.3 eV and below −3.0 eV, respectively. The dynamical stabilities of s-GB, r-GB, p-GB have been examined by performing molecular dynamics. All the GB structures at the equilibrated phases (Fig. S2 online) were well maintained.

To provide the detailed synthesis conditions of temperature and pressure, the phase diagram of the Σ5(2 1 0) GB of rutile TiO_2 under different O atmospheres were calculated. The contribution of temperature and pressure to the free energies of the solid-state phases, including E_{interf}, E_{ref}, $E_{\text{Ti(bulk)}}$ and $\Delta H_{\text{f}}(\text{TiO}_2)$ in Eq. (15) can be negligible [57]. The variation in the chemical potential of O relative to the value at 0 K under given temperature T and pressure P, $\Delta\mu_{\text{O}}(T,P)$, can be defined using the ideal gas expression [57]:

$$\Delta\mu_{\text{O}}(T,P) = \frac{1}{2}T\left[C_{\text{p}}^{0} - S_{\text{O}_2}^{0} - C_{\text{p}}^{0}\ln\left(\frac{t}{t_0}\right) + k_{\text{B}}\ln\left(\frac{p}{p_0}\right)\right], \quad (16)$$

where t_0 = 298.15 K and p_0 = 1 atm (1 atm = 1.013×10^5 Pa). C_{p}^{0} was the constant-pressure specific heat capacity per diatomic molecule and equals $(7/2)k_{\text{B}}$. $S_{\text{O}_2}^{0}$ represented the standard entropy (205 J/(mol·K)) [58]. The calculated phase diagram as a function of temperature and O partial pressure was plotted in Fig. 5b. The results indicate that p-GB are stable under the more reducing atmosphere (higher temperature or lower O partial pressure) compared with r-GB. The stabilizing temperature for r-GB and p-GB increases with increasing O partial pressure. In particular, under a standard vacuum pressure (10^{-10} atm), r-GB and p-GB become stable at 1,111 and 1,405 K, respectively.

The predicted structures of s-GB, r-GB, and p-GB were presented in Fig. 5c–e. All three stable GB structures are asymmetric with a rigid-body displacement between two grains. The local coordination environments in s-GB are consistent with those in the bulk phase, where Ti and O are six-coordinated and three-

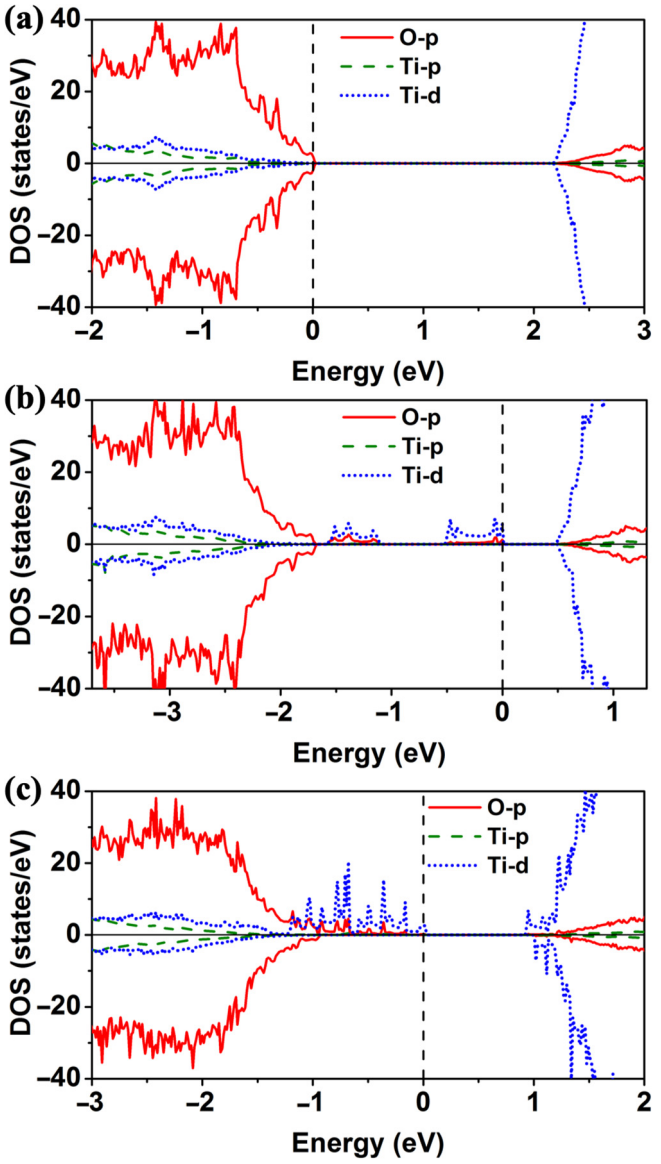

Fig. 6. (Color online) Calculated PDOS of (a) s-GB, (b) r-GB, and (c) p-GB configurations. The black dashed line indicates the Fermi level.

coordinated, respectively. Unlike s-GB, the predicted GBs of r-GB and p-GB are O-deficient phases, where Γ_O is −2 and −4, respectively, suggesting that the O defects are significantly gathered at these two GBs. For r-GB, all the O atoms at GB are four-fold coordinated to Ti, sharing similarity in the local coordination environment with the defective rutile bulk structure with Ti interstitials [57]. In p-GB, except for the four-coordinated O atoms, the five-coordinated O atoms and five-coordinated Ti atoms appear at the GB because of the severe O deficiency of GB.

The spin-polarized projected densities of states (PDOS) for s-GB, r-GB, and p-GB were calculated and depicted in Fig. 6. For s-GB, the band gap is approximately 2.1 eV (Fig. 6a), which is almost the same with the theoretical results for the rutile bulk phase [59]. The two occupied Ti-3*d* states induced from the O defects are localized in the band gap for r-GB (Fig. 6b), which are lower than the conduction band maximum by 0.75 and 1.8 eV, respectively. The projected charge densities associated with these interfacial defect states (Fig. S3a online) are strongly localized at Ti cations at GBs, leading to the reduction of Ti^{4+} to Ti^{3+} ions. These localized interfacial states are similar to the defect states induced from O vacancies and Ti interstitials in the rutile bulk phase [57]. Because of the strong hybridization, the Ti-3*d* interfacial levels localized at Ti^{3+} centers at p-GB (Fig. S3b online) are substantially broader than the localized impurity levels in r-GB, forming intermediate bands. Consequently, the intrinsic band gap is narrowed to 0.7 eV (Fig. 6c). A similar phenomenon has also been observed in deficient ZnO with a high concentration of O vacancies [60]. The bandgap narrowing may be promising for energy conversion applications involving the solar spectrum and enhancing the photocatalytic performance of TiO_2.

4. Conclusion

A robust and generalized method for predicting solid–solid interface structures based on the CALYPSO methodology was proposed, and several specially designed techniques were employed to significantly improve its search efficiency. This method was validated by successfully reproducing the known interface structures of graphene armchair-zigzag GB and Σ3(1 1 2) GB of rutile TiO_2 with only given information of interfacial atomic compositions and two parent solids. Using the proposed method, we discovered two novel stable GB structures (r-GB and p-GB) containing Ti^{3+} originating from O defects in Σ5(2 1 0) GBs of rutile TiO_2 under a reducing atmosphere. Our calculations indicate that the Ti^{3+} existing in the predicted GB structures can narrow the band gap and may be beneficial for improving the visible-light photoactivity of TiO_2. In summary, the proposed method provides an invaluable tool to determine the atomic structures of interfaces, thereby opening a door toward the design of novel interface materials with an exceptionally high figure of merit.

Conflict of interest

The authors declare that they have no conflict of interest.

Acknowledgments

This work was supported by the National Natural Science Foundation of China (11774127, 11822404 and 11534003), the National Key Research and Development Program of China (2016YFB0201200, 2016YFB0201201, and 2016YFB0201204), the Program for JLU Science and Technology Innovative Research Team (JLUSTIRT), and the Science Challenge Project (TZ2016001). Part of the calculation was performed in the High Performance Computing Center of Jilin University and at Tianhe2-JK in the Beijing Computational Science Research Center.

Author contributions

Y. M. designed the research. B. G performed most of the calculations. B. G, P. G, and S. L coded the interface structure prediction method into CALYPSO. B. G, P. G, J. L, Y. W, and Y. M analyzed the results and wrote the manuscript. All authors commented on the manuscript.

Appendix A. Supplementary data

Supplementary data to this article can be found online at https://doi.org/10.1016/j.scib.2019.02.009.

References

[1] Ohtomo A, Hwang HY. A high-mobility electron gas at the $LaAlO_3/SrTiO_3$ heterointerface. Nature 2004;427:423–6.
[2] Khang DY. Grain boundary strengthening in alumina by rare earth impurities. Science 2006;311:208–12.
[3] Li C, Wu Y, Poplawsky J, et al. Grain-boundary-enhanced carrier collection in CdTe solar cells. Phys Rev Lett 2014;112:156103.
[4] Haruyama J, Sodeyama K, Han L, et al. Space–charge layer effect at interface between oxide cathode and sulfide electrolyte in all-solid-state lithium-ion battery. Chem Mater 2014;26:4248–55.
[5] Raghunathan R, Johlin E, Grossman JC. Grain boundary engineering for improved thin silicon photovoltaics. Nano Lett 2014;14:4943–50.
[6] Ricci PC, Carbonaro CM, Stagi L, et al. Anatase-to-rutile phase transition in TiO_2 nanoparticles irradiated by visible light. J Phys Chem C 2013;117:7850–7.
[7] Sun R, Wang Z, Saito M, et al. Atomistic mechanisms of nonstoichiometry-induced twin boundary structural transformation in titanium dioxide. Nat Commun 2015;6:7120.
[8] Yu Q. Control and characterization of individual grains and grain boundaries in graphene grown by chemical vapour deposition. Nat Mater 2011;10:443–9.
[9] Chen Y, Washburn J. Structural transition in large-lattice-mismatch heteroepitaxy. Phys Rev Lett 1996;77:4046–9.
[10] Tang H, Deng Z, Lin Z, et al. Probing solid–solid interfacial reactions in all-solid-state sodium-ion batteries with first-principles calculations. Chem Mater 2017;30:163–73.
[11] Chua ALS, Benedek NA, Chen L, et al. A genetic algorithm for predicting the structures of interfaces in multicomponent systems. Nat Mater 2010;9:418–22.
[12] Zhao X, Shu Q, Nguyen MC, et al. Interface structure prediction from first-principles. J Phys Chem C 2014;118:9524–30.
[13] Li ZL, Li ZM, Cao HY, et al. What are grain boundary structures in graphene? Nanoscale 2014;6:4309–15.
[14] Schusteritsch G, Pickard CJ. Predicting interface structures: from $SrTiO_3$ to graphene. Phys Rev B 2014;90:035424.
[15] Zhu Q, Samanta A, Li B, et al. Predicting phase behavior of grain boundaries with evolutionary search and machine learning. Nat Commun 2018;9:467.
[16] Kiyohara S, Oda H, Miyata T, et al. Prediction of interface structures and energies via virtual screening. Sci Adv 2016;2. e1600746.
[17] Wang Y, Lv J, Zhu L, et al. Crystal structure prediction via particle-swarm optimization. Phys Rev B 2010;82:094116.
[18] Wang Y, Lv J, Zhu L, et al. CALYPSO: a method for crystal structure prediction. Comput Phys Commun 2012;183:2063–70.
[19] Wang Y, Ma Y. Perspective: crystal structure prediction at high pressures. J Chem Phys 2014;140:040901–40912.
[20] Wang Y, Lv J, Zhu L, et al. Materials discovery via CALYPSO methodology. J Phys: Condens Matter 2015;27:203203–15.
[21] Wang H, Wang Y, Lv J, et al. CALYPSO structure prediction method and its wide application. Comp Mater Sci 2016;112:406–15.
[22] Wang Y, Miao M, Lv J, et al. An effective structure prediction method for layered materials based on 2D particle swarm optimization algorithm. J Chem Phys 2012;137:224108–17.
[23] Lv J, Xu M, Lin S, et al. Direct-gap semiconducting tri-layer silicene with 29% photovoltaic efficiency. Nano Energy 2018;51:489–95.
[24] Zhu L, Liu H, Pickard CJ, et al. Reactions of xenon with iron and nickel are predicted in the Earth's inner core. Nat Chem 2014;6:644–8.
[25] Lv J, Wang Y, Zhu L, et al. Particle-swarm structure prediction on clusters. J Chem Phys 2012;137:084104.
[26] Lv J, Wang Y, Zhu L, et al. B38: an all-boron fullerene analogue. Nanoscale 2014;6:11692–6.
[27] Lu S, Wang Y, Liu H, et al. Self-assembled ultrathin nanotubes on diamond (100) surface. Nat Commun 2014;5:3666.
[28] Gao B, Shao X, Lv J, et al. Structure prediction of atoms adsorbed on two-dimensional layer materials: method and applications. J Phys Chem C 2015;119:20111–8.

[29] Lu J, Gomes LC, Nunes RW, et al. Lattice relaxation at the interface of two-dimensional crystals: graphene and hexagonal boron-nitride. Nano Lett 2014;14:5133–9.
[30] Stradi D, Jelver L, Smidstrup S, et al. Method for determining optimal supercell representation of interfaces. J Phys: Condens Matter 2017;29:185901–8.
[31] Jelver L, Larsen PM, Stradi D, et al. Determination of low-strain interfaces via geometric matching. Phys Rev B 2017;96:085306–85307.
[32] Lazić P. Cell match: combining two unit cells into a common supercell with minimal strain. Comput Phys Commun 2015:1–25.
[33] Mathew K, Singh AK, Gabriel JJ, et al. MPInterfaces: a materials project based Python tool for high-throughput computational screening of interfacial systems. Comp Mater Sci 2016;122:183–90.
[34] Park RL, Madden HH. Annealing changes on the (100) surface of palladium and their effect on CO adsorption. Surf Sci 1968;11:188–202.
[35] Ju MG, Sun G, Wang J, et al. Origin of high photocatalytic properties in the mixed-phase TiO_2: a first-principles theoretical study. ACS Appl Mater Interfaces 2014;6:12885–92.
[36] Brown ID. The chemical bond in inorganic chemistry: the bond valence model. Oxford University Press; 2016.
[37] Aradi B, Hourahine B, Frauenheim T. DFTB+, a sparse matrix-based implementation of the DFTB method. J Phys Chem A 2007;111:5678–84.
[38] Köhler C, Frauenheim T. Molecular dynamics simulations of CFx (x = 2,3) molecules at Si_3N_4 and SiO_2 surfaces. Surf Sci 2006;600:453–60.
[39] Kresse G, Joubert D. From ultrasoft pseudopotentials to the projector augmented-wave method. Phys Rev B 1999;59:1758–75.
[40] Blöchl PE. Projector augmented-wave method. Phys Rev B 1994;50:17953–79.
[41] Luschtinetz R, Frenzel J, Milek T, et al. Adsorption of phosphonic acid at the TiO_2 anatase (101) and rutile (110) surfaces. J Phys Chem C 2009;113:5730–40.
[42] Morgan BJ, Watson GW. A DFT+U description of oxygen vacancies at the TiO_2 rutile (110) surface. Surf Sci 2007;601:5034–41.
[43] Howard CJ, Sabine TM, Dickson F. Structural and thermal parameters for rutile and anatase. Acta Crystallogr B Struct Sci 1991;47:462–8.
[44] Liu Y, Yakobson BI. Cones, pringles, and grain boundary landscapes in graphene topology. Nano Lett 2010;10:2178–83.
[45] Jin Z, Zhang X, Lu G, et al. Improved quantum yield for photocatalytic hydrogen generation under visible light irradiation over eosin sensitized TiO_2—investigation of different noble metal loading. J Mol Catal A: Chem 2006;259:275–80.
[46] Asahi R, Morikawa T, Irie H, et al. Nitrogen-doped titanium dioxide as visible-light-sensitive photocatalyst: designs, developments, and prospects. Chem Rev 2014;114:9824–52.
[47] Zhou W, Li W, Wang JQ, et al. Ordered mesoporous black TiO_2 as highly efficient hydrogen evolution photocatalyst. J Am Chem Soc 2014;136:9280–3.
[48] Xu M, Shao S, Gao B, et al. Anatase (101)-like structural model revealed for metastable rutile TiO_2 (011) surface. ACS Appl Mater Interfaces 2017;9:7891–6.
[49] Zuo F, Wang L, Wu T, et al. Self-doped Ti^{3+} enhanced photocatalyst for hydrogen production under visible light. J Am Chem Soc 2010;132:11856–7.
[50] Wan Z, Huang GF, Huang WQ, et al. The enhanced photocatalytic activity of Ti^{3+} self-doped TiO_2 by a reduction method. Mater Lett 2014;122:33–6.
[51] Bryan JD, Santangelo SA, Keveren SC, et al. Activation of high-T_c ferromagnetism in Co^{2+}:TiO_2 and Cr^{3+}:TiO_2 nanorods and nanocrystals by grain boundary defects. J Am Chem Soc 2005;127:15568–74.
[52] Wei Y, Zhou Z, Fang W-H, et al. Grain boundary facilitates photocatalytic reaction in rutile TiO_2 despite fast charge recombination: a time-domain ab initio analysis. J Phys Chem Lett 2018;9:5884–9.
[53] Körner W, Elsässer C. Density functional theory study of dopants in polycrystalline TiO_2. Phys Rev B 2011;83:205315.
[54] Sinnott SB, Wood RF, Pennycook SJ. Ab initio calculations of rigid-body displacements at the Σ5 (210) tilt grain boundary in TiO_2. Phys Rev B 2000;61:15645–8.
[55] Dawson I, Bristowe PD, Lee MH, et al. First-principles study of a tilt grain boundary in rutile. Phys Rev B 1996;54:13727–33.
[56] Wallis DJ, Browning ND, Nellist PD. Atomic structure of a 36.8 (210) tilt grain boundary in TiO_2. J Am Ceram Soc 1997;80:499–502.
[57] Morgan BJ, Watson GW. Intrinsic n-type defect formation in TiO_2: a comparison of rutile and anatase from GGA+ U calculations. J Phys Chem C 2010;114:2321–8.
[58] Reuter K, Scheffler M. Composition, structure, and stability of RuO_2(110) as a function of oxygen pressure. Phys Rev B 2001;65:1038–111.
[59] Hu Z, Metiu H. Choice of U for DFT+U calculations for titanium oxides. J Phys Chem C 2011;115:5841–5.
[60] Wang J, Wang Z, Huang B, et al. Oxygen vacancy induced band-gap narrowing and enhanced visible light photocatalytic activity of ZnO. ACS Appl Mater Interfaces 2012;4:4024–30.

Bo Gao received his B.Sc. degree from the College of Physics, Jilin University in 2012, and Ph.D. degree from State Key Laboratory of Superhard Materials, Jilin University in 2017. He is currently a postdoctor researcher in the National Institute for Materials Science, Japan. His research interests focus on the development of the highly efficient structure prediction method, and its application for the theoretical prediction and design of novel surfaces and interfaces.

Yanming Ma received his Ph.D. degree from Jilin University in 2001, and then spent several years in National research council of Canada and ETH of Zurich for postdoctoral researches. He is currently a distinguished Changjiang Professor and Dean of College of Physics in Jilin University. His research interests mainly focus on the development of simulation methods on structure prediction and large-scale electronic structure calculations, and the use of these developed methods to explore phase structures and exciting physics of condensed matters under high pressure.